UC Irvine
UC Irvine Previously Published Works

Title

Reactive impinging-flow technique for polymer-electrolyte-fuel-cell electrode-defect detection

Permalink

https://escholarship.org/uc/item/4mx4k9rd

Authors

Zenyuk, Iryna V
Englund, Nicholas
Bender, Guido
et al.

Publication Date

2016-11-01

DOI

10.1016/j.jpowsour.2016.09.109

Peer reviewed

Reactive impinging-flow technique for polymer-electrolyte-fuel-cell electrode-defect detection

Iryna V. Zenyuk [a, c], Nicholas Englund [a], Guido Bender [b], Adam Z. Weber [a], Michael Ulsh [b, *]

[a] Energy Conversion Group, Energy Technologies Area, Lawrence Berkeley National Laboratory, Berkeley, CA 94720, USA
[b] National Renewable Energy Laboratory, Golden, CO 80401, USA
[c] Department of Mechanical Engineering, Tufts University, Medford, MA 02155, USA

HIGHLIGHTS

- Noninvasive technique defect detection in roll to roll electrodes identified.
- Modeling and experiments demonstrate optimal operating conditions for diagnostic.
- Infrared imaging with hydrogen excitation detects all GDE defects.

ARTICLE INFO

ABSTRACT

Reactive impinging flow (RIF) is a novel quality-control method for defect detection (i.e., reduction in Pt catalyst loading) in gas-diffusion electrodes (GDEs) on weblines. The technique uses infrared thermography to detect temperature of a nonflammable ($<4\%$ H_2) reactive mixture of H_2/O_2 in N_2 impinging and reacting on a Pt catalytic surface. In this paper, different GDE size defects (with catalyst-loading reductions of 25, 50, and 100%) are detected at various webline speeds (3.048 and 9.144 m min^{-1}) and gas flowrates (32.5 or 50 standard L min^{-1}). Furthermore, a model is developed and validated for the technique, and it is subsequently used to optimize operating conditions and explore the applicability of the technique to a range of defects. The model suggests that increased detection can be achieved by recting more of the impinging H_2, which can be accomplished by placing blocking substrates on the top, bottom, or both of the GDE; placing a substrate on both results in a factor of four increase in the temperature differential, which is needed for smaller defect detection. Overall, the RIF technique is shown to be a promising route for in-line, high-speed, large-area detection of GDE defects on moving weblines.

© 2016 Elsevier B.V. All rights reserved.

1. Introduction

The development of the production of membrane-electrode-assembly (MEA) components using roll-to-roll processes [1–4] has resulted in overall polymer-electrolyte-fuel-cell (PEFC) cost reduction and production with improved throughput and repeatability [5,6]. For continuous processes, such as roll-to-roll, quality control during MEA component manufacturing has been identified as a critical issue [7,8]. Quality control for the moving two-dimensional functional surface, such as a gas-diffusion electrode (GDE), is challenging because the surface is in continuous motion and because of underlying heterogeneities across the GDE. A GDE sheet consists of a Pt-containing catalyst ink deposited on a porous carbon substrate (*i.e.* gas diffusion layer (GDL)). As the Pt electro-catalyst is a high-cost contributor to a PEFC stack, maximizing yield during production is of high importance. In addition, uniformity of catalyst-layer (CL) thickness is crucial for optimal PEFC cell performance [9–11]. Moreover, formation of cracks, voids and other mechanical defects in the GDE produced during a high throughput coating process can result in premature cell failure and component degradation [9,12–14].

Several rapid, nondestructive quality-control techniques are available for in-line defect detection for a GDE fabricated under a continuous process. Optical inspection of visible defects and measurements of coating thickness are used in the PEFC industry [15]. These techniques are limited in their applicability, as not all defects are visible, and offer limited probing depth due to light scattering [16]. More recently, X-ray Fluorescence (XRF) spectroscopy has

been applied for measuring GDE Pt loading in-line [17,18]. However, XRF is a point measurement, and commercial systems are hindered by a slow acquisition time, thus inspecting a full 100% of GDE area is not feasible in real-time.

Infrared (IR) thermography with active excitation of the GDE material is a nondestructive evaluation tool that allows for complete, rapid, and noncontact defect detection [19–21]. We have demonstrated the feasibility of IR thermography coupled with direct-current (DC) electronic-excitation of catalyst-coated membranes [22] on an industrial-scale webline and reactive-flow-through (RFT) [23,24] excitation on stationary, enclosed GDEs. For RFT, a nonflammable (<4% H_2) reactive mixture of H_2/O_2 in N_2 is flowed through the GDE where the catalytic reaction on the Pt surface generates heat, creating a measurable thermal signature. A proof-of-concept of the extension of the RFT technique to an open-atmosphere environment, where the GDE is conveyed on a bench-top roller system, was previously reported and termed as reactive impinging flow (RIF) [25]. In this work, we report on the further development of the IR thermography technique coupled with RIF to detect defects in moving GDEs. In particular, we describe the transfer of the technique from a bench-top roller system to a research webline both experimentally and theoretically. For the latter, mathematical modeling is used to assess the optimal operation window for defect detection and explore the parameter space. Compared to the prior modeling work of RFT [10], the model developed in this work captures the physics of impinging flow onto the porous GDE on a moving webline. Moreover, this manuscript builds upon RIF technique demonstration [25] and explores optimal parametric space for webline velocity, gas flowrate, composition, and defect geometry for defect detectability. It also provides recommendations for improved defect detection using RIF technique.

The outline of the paper is as follows. First, the experimental setup of the research webline and fabricated GDEs are presented. Then, the model geometric domains, approximations, and physics are explained. Model calibration is performed against the thermal response of the pristine GDE on the stationary and moving weblines. Then, the detectability of defects is explored with the experiments and model parametric study. Lastly, methods to increase hydrogen utilization and improve defect detectability is discussed.

2. Experimental

The experimental work presented below was performed on an industrial-style roll-to-roll system built by Davis-Standard, which includes unwind and rewind stations to unroll; control speed, tension, and steering; and reroll sheet or roll material. Between the unwind and rewind stations, an experimental station is positioned, whereupon the RIF experimental components and infrared sensor were mounted. The line can handle web material up to 0.46 m width at speeds of 0.305–30.5 m min^{-1} and tensions of 87.6–876 N m^{-1}. An image of the webline, threaded-up with the GDE sheet fabricated for these experiments, is shown in Fig. 1.

The GDE sheet was fabricated in-house, such that it contained a variety of CL defects, by spraying Pt-containing catalyst ink onto a GDL substrate. The catalyst ink contained 49.5 wt% Pt/C catalyst from Tanaka (TKK TEC10E50E), 20 wt% Nafion® solution with 1100 EW from Ion Power, de-ionized water, and n-propanol. The Nafion®/carbon weight ratio of the ink was adjusted to 0.8. The ink was sprayed onto the substrate using a Sono-tek ExactaCoat spray system with a programmable 3D robotic gantry and a 25 kHz Sono-tek Accumist ultrasonic spray head. The nominal loading of the sprayed CL was 0.13 mg-Pt cm^{-2}. The substrate was an

approximately 10 m long by 0.15 m wide sheet of GDL with a microporous layer (MPL) coating from AvCarb, LLC (formerly Ballard Material Products). Onto the midsection of the substrate, three successive 0.14 × 0.25 m sections of CL were sprayed, each having a different set of defects. Each section had five square defects, of sizes 0.0625, 0.13, 0.25, 0.5, and 1.0 cm^2. In one section, each defect had a 100% reduction in CL thickness, i.e. each defect was a bare spot. In another section, each defect had a 50% reduction in the CL thickness. And in the third section, each defect had a 25% reduction in the CL thickness. Thus, 15 defects were intentionally created of different size and thickness reduction. Fig. 1c shows a diagram of the sprayed section of the GDL sheet. Defects were created by masking the desired defect size during the spray process, as can be seen in Fig. 1d. The desired reduction in thickness was achieved by placing the mask on the surface for the appropriate fraction of the final spray passes, e.g. the last quarter of the passes for a 25% reduction of CL thickness. Fig. 1e shows an image of the defect sections of the GDE at 100% CL reduction. No figure is shown for the 25% CL reduction defect section, as the defects were not visible either by eye or optical imaging. The reader can appreciate that CL defects of <100% reduction consist of a discrete black area within a black surface, and thus are not easily detected by optical methods.

Fig. 1b provides a schematic diagram of the setup for the RIF webline experiments. Experiments were performed using a non-flammable gas mixture containing 2% H_2 and 1% O_2 in N_2. This gas mixture was chosen as a balance between maximizing the thermal response from the CL [23] and maintaining a safe, i.e. nonflammable, mixture. The gas mixture was delivered from a pressurized gas cylinder to the GDE surface through a gas knife using a bench-top MKS gas-flow-control system. A rectangular stainless steel plenum was used as the gas knife for these experiments. The knife had a linear array of laser drilled circular holes of 0.5 mm diameter with center-to-center spacing of 2 mm and a total cross-web length of 0.33 m. Reproducible positioning of the gas knife relative to the GDE surface was achieved by using micrometer screws with digital readouts that were integrated into the knife mounting assembly. Alignment of the gas knife relative to the cross-web direction was accomplished by shining light through the holes of the gas knife with a specially designed light source.

During all of the experiments, the GDE was oriented with the CL facing toward the IR camera and impinging gas flow. The operating conditions for the experiments were: (i) gas flowrate of 32.5 or 50 standard L min^{-1}, (ii) line speed of 3.048 or 9.144 m min^{-1}, (iii) substrate tension of 87.6 N m^{-1}, and (iv) 1 mm gas knife height from the GDE surface. The line speed used was intended to reflect current or near-term industry practice with regard to coating PEFC electrodes.

An IR camera (Jenoptik Vario-Cam HiRes) with a 640 by 480 pixel uncooled microbolometer detector was employed to capture the thermal signature of the GDE. The spectral range of the camera was 7.5–14 μm and its thermal resolution was 0.030 K. The viewing angle of the camera was orthogonal to the substrate. The camera was positioned downstream from the gas knife, relative to the motion of the substrate, at a height above the GDE surface such that the field of view included the gas knife and the excited GDE. IR data collected at a frame rate of 60 frames s^{-1} were captured with Thermography Suite (IRCameras, Inc.) software. Data consisted of time and temperature information for each pixel recorded with the IR detector. A uniform emissivity of 0.95 was used for the GDE. This value was determined using a comparative method [26] wherein the surface temperature of the GDE measured with the IR camera at a set temperature is compared to a material of known emissivity at the same temperature.
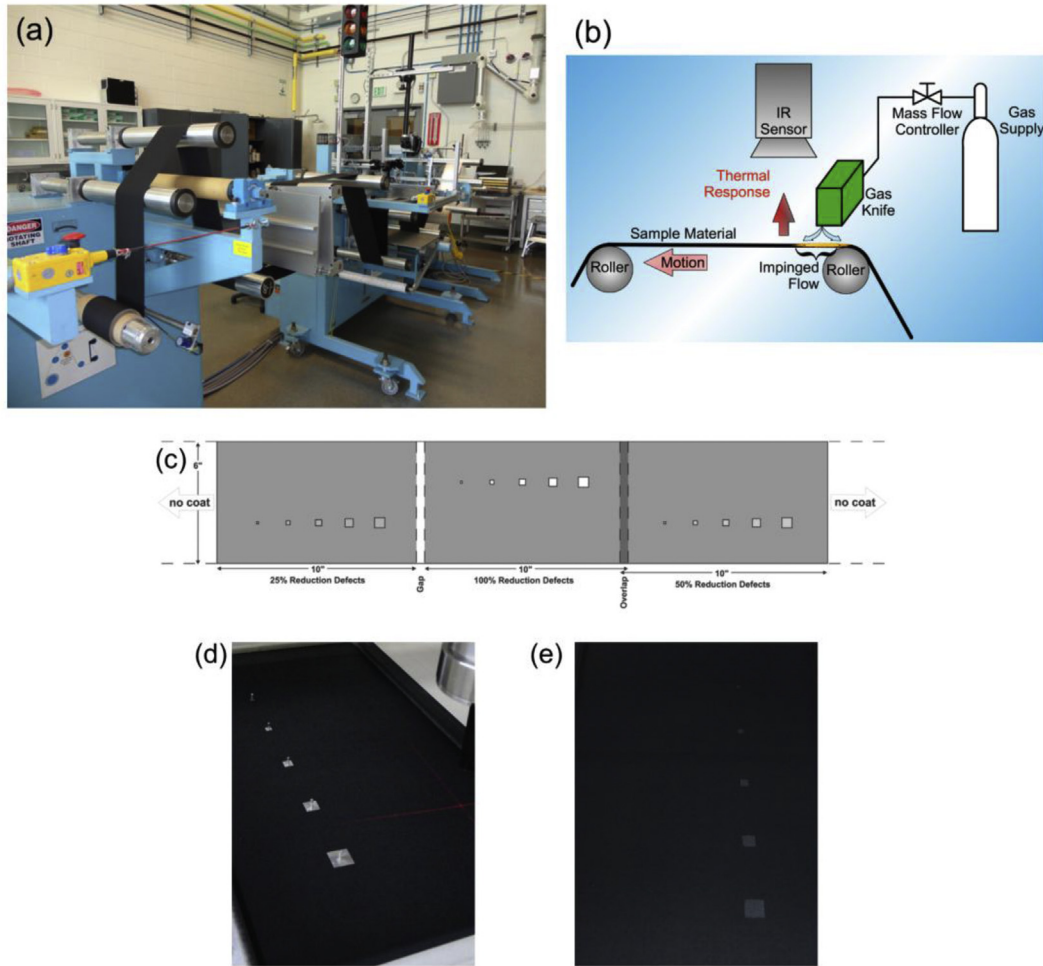
Fig. 1. A) The NREL research webline with GDE sheet. The rewind station is on the front left, the experimental station in the middle, and the unwind on the far right. b) Schematic of the RIF experimental setup. c) Ultrasonically sprayed GDE sample showing three different defect sections that contain five defects each and two different interface sections. d) GDE sample during fabrication showing the five metal masks used for thickness reduction defect creation. e) Section of GDE sample that contains five defects of various sizes featuring 100% loading reduction.

3. Model formulation

To guide the experiments, identify optimal conditions of web-line velocity and gas-mixture flowrate, and explore the limits of the technique relative to not easily experimentally accessible parameter space, a computational model was developed. The model was based on initial work by Das et al. [10] that was developed for stationary, enclosed GDEs. Here, additional fluid-dynamics complexities were included related to the open-atmosphere environment, impinging flow into the porous GDE, and moving webline. Fig. 2a shows a schematic of the model computational domains that include the air and the GDE porous domains (CL, MPL, and GDL). The model is two-dimensional and built to simulate the cross-section of the knife with a gas-flow from a single injection hole, i.e. in the down-web direction, or direction of GDE motion.

The model developed here captures the underlying complex interplay between several mass and thermal processes occurring simultaneously. A sample temperature distribution is depicted in Fig. 2b, where heat generated in the chemical reaction (reaction heat) depends on the impinged hydrogen concentration and temperature, and where convective cooling is a function of impinging flow velocity. The highest generated reaction heat is at the flow impinging point where there is high H_2 concentration; however,

this point also is the location with the highest impinging gas-flow velocity onto the GDE surface and therefore convective cooling is the highest. Depending on the relative magnitudes between the two heat-transfer phenomena, the temperature profile can either have a peak (for low flowrates) or valley (for high flowrates, when convection is significant) at the impingement point.

3.1. Governing equations

The modeled physics are represented with a set of second-order differential equations that include time-dependence, however, here only steady-state solutions are presented. Navier-Stokes and continuity equations describe the flow of gas from the gas-knife that is comprised of a mixture of 2% H_2, 1% O_2 and balance nitrogen,

$$\rho(\boldsymbol{u}\cdot\nabla\boldsymbol{u}) = -\nabla P + \nabla\cdot(\mu\nabla\boldsymbol{u}) \tag{1}$$

$$\nabla\cdot(\rho\boldsymbol{u}) = 0 \tag{2}$$

where ρ, μ, $\boldsymbol{u}$, and P are the gas density, viscosity, velocity, and pressure, respectively.

Continuity with Brinkman's equation are used to describe viscous flow in the porous domains (CL, MPL, and GDL),
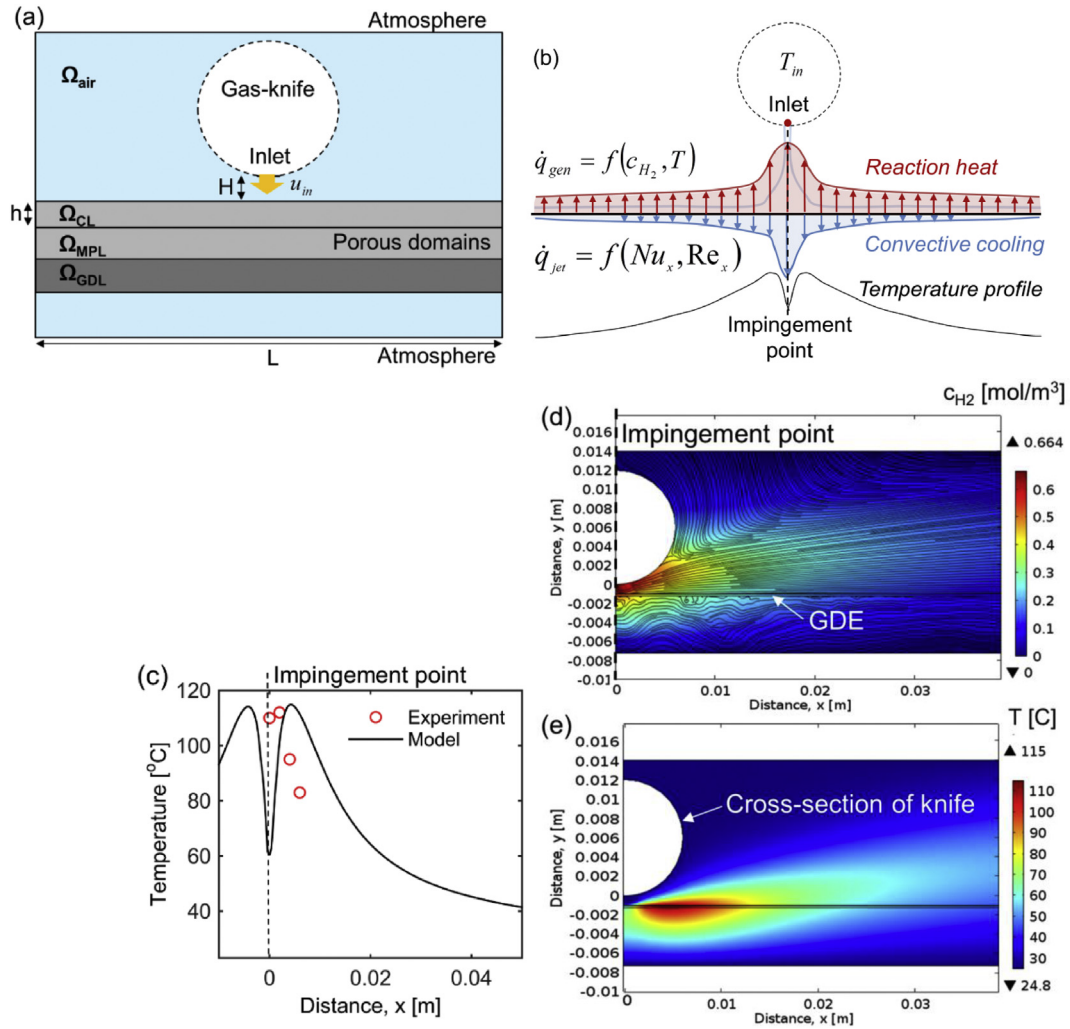
Fig. 2. a) Schematic of the model domains (not to scale) and b) schematic of heat signature of the GDE and a corresponding temperature profile. **c**) Model temperature profile compared to the experimental data. d) 2D plot of hydrogen concentration with flow streamlines and e) 2D plot of temperature profile.

$$\mu \nabla^2 \boldsymbol{u} - \frac{\mu}{\kappa} \boldsymbol{u} - \nabla P = 0 \qquad [3]$$

$$\nabla \cdot (\rho \boldsymbol{u}) = 0 \qquad [4]$$

where κ is the effective permeability of the porous medium.

To account for H_2, O_2 and N_2 diffusion, transport of diluted species with convection is applied in air and the porous domains,

$$\frac{\partial c_i}{\partial t} + \nabla \cdot \left(-D_{i,eff} \nabla c_i \right) + \boldsymbol{u} \cdot \nabla c_i = R_i \qquad [5]$$

$$\boldsymbol{N}_i = -D_{i,eff} \nabla c_i + \boldsymbol{u} c_i$$

where c_i is the molar concentration of species i, R_i is a production/consumption term for gas species i, and $D_{i,eff} = \varepsilon^m D_i$ is the effective gas-phase diffusivity adjusted for porosity and tortuosity in the porous domains, where the Bruggeman coefficients, m, for each porous domain are reported in Table 1. The model assumes thermal equilibrium between gas and solid phases. Conservation of energy is used to find the temperature, T, distribution.

$$\left(\rho C_p \right)_{eff} \frac{\partial T}{\partial t} + \rho C_p \boldsymbol{u} \cdot \nabla T + \nabla \left(-k_{eff} \nabla T \right) = rh_{comb} \qquad [6]$$

where C_p is the specific heat capacity and k is the thermal conductivity. On the right side, the source term is due to the heat generated by chemical reaction, where $h_{comb} = 120$ $[MJkg^{-1}]$ is the lower heating value for hydrogen. The effective volumetric heat capacity, $(\rho C_p)_{eff}$, for the porous domains is a combination of the solid heat capacity, $(\rho C_p)_s$, and that for gas mixture, $(\rho C_p)_g$:

$$\left(\rho C_p \right)_{eff} = (1 - \varepsilon)\left(\rho C_p \right)_s + \varepsilon \left(\rho C_p \right)_g \qquad [7]$$

Similarly, the effective thermal conductivity for the porous domains is expressed as

Table 1
Porous domains properties.

Parameters	GDL	MPL	CL
Length, L [mm]	180	180	180
Thickness, h [μm]	190	45	9
Porosity	0.8	0.3	0.3
Permeability [m²]	1.14×10^{-11}	1.54×10^{-14}	2.3×10^{-15}
Bruggeman factor, m	2.2 [29]	1.5	1.5

Table 2
Operating conditions and model parameters.

Parameters	Value
Inlet gas-flow temperature, T_{in} [K]	298
Inlet pressure (atmospheric in Denver), P_{in}, P_{atm} [Pa]	82,000
Molar fraction of inlet hydrogen on percentage basis, $x_{H_2, in}$[%]	2
Molar fraction of inlet oxygen on percentage basis, $x_{O_2, in}$ [%]	1
Kinetic rate constant, B [ms^{-1}]	14
Fitting parameter, A_v [m^{-1}]	1×10^5
Reaction activation energy E [Jmol^{-1}]	14.9×10^3

$$k_{eff} = (1 - \varepsilon)k_s + \varepsilon k_g \qquad [8]$$

The gas mixture density, specific heat capacity, and thermal conductivity are estimated assuming ideal-gas properties.

The chemical reaction rate, r, is approximated as a one-step combustion reaction of hydrogen and oxygen [27], where the activation energy is assumed to be constant and corresponds to that of a lean flame,

$$r = A_v B c_{H_2}^{\alpha} \exp\left(-\frac{E}{RT}\right) \qquad [9]$$

The activation energy, E, reaction-rate constant, B, hydrogen reaction order, α, and a fitting parameter, A_v, to account for inter-facial surface area to volume ratio, are reported in Table 2 [27]. The hydrogen reaction order and A_v were adjusted to calibrate the model against the experimental data. A calibration point was chosen from the experimental data for a stationary web and jet velocity of 32.5 standard L min^{-1}. Then α, and A_v were varied to fit the magnitude of temperature peaks and their location.

3.2. Boundary conditions

The modeling air domains were simulated to be sufficiently large such that the horizontal length of the domain was much larger than the diameter of the gas nozzle [28] to represent atmospheric conditions. For the Navier-Stokes equations, the pressure on the outer boundaries of the air domains was set to atmospheric. No-slip boundary condition was applied along the gas-knife walls,

$$\boldsymbol{u} = 0 \qquad [10]$$

The velocity of the inlet gas was set to 0 in the x-direction and that to the inlet velocity in the y-direction. The inlet velocity was computed from the volumetric flowrate through the knife divided by the number of injection holes in the gas-knife and hole area to get velocity per single injection hole. Navier-Stokes equations in the air domains and Brinkman's equations in the porous domains were coupled via boundary conditions on the porous domains through a continuous velocity y-direction component:

$$\boldsymbol{u_{air.y}} = \boldsymbol{u_{p.y}} \qquad [11]$$

with the x-direction velocity component set to 0 (no-slip) for a stationary web and to the web velocity for a moving webline.

For the dilute-mixture transport equations, a no-flux boundary condition was set at the knife edge. The inlet molar concentrations for oxygen, c_{O_2}, hydrogen, c_{H_2}, and nitrogen, c_{N_2}, were specified based on their inlet molar fractions:

$$c_{H_2} = \frac{x_{H_2, in}P_{in}}{N_A k T_{in}}$$

$$c_{O_2} = \frac{x_{O_2, in}P_{in}}{N_A k T_{in}} \qquad [12]$$

$$c_{N_2} = \frac{(1 - x_{H_2, in} - x_{O_2, in})P_{in}}{N_A k T_{in}}$$

The inlet pressure, P_{in}, and temperature, T_{in}, are reported in Table 2. At the outer boundaries of the air domains, the molar-concentration boundary conditions were set to those of air (i.e., 0% H$_2$, 21% O$_2$, 79% N$_2$) at atmospheric pressure (in Denver) and temperature.

For the energy-conservation equation, the temperature at the outer boundaries of the air domains was set to atmospheric:

$$T = T_{atm} \qquad [13]$$

3.3. Model parameters and numerical method

Table 2 reports the model parameters, where the operating conditions were chosen to those of the experimental data. COMSOL Multiphysics 5.1 (COMSOL, Inc., Palo Alto, CA) was used to solve the coupled physics equations with a steady-state solver. The porous domains were meshed with quadrilateral elements, with 600 elements along the x-direction and a total number of 15,150 elements. The air domains were meshed with triangular elements, with a total mesh number of 16,755. Larger mesh density in the porous domains was selected due to their high aspect ratio and also due to high reaction fluxes that can possibly introduce numerical instability. The fully-coupled physics were solved with the direct MUMPS solver.

3.4. Model validation

To ensure that the model physics and boundary conditions are implemented correctly and that the mesh density is satisfactory we validated the fluid dynamics computational module against analytical solution. Here we provide salient details, whereas in-depth overview is presented in Supplementary Material. A simplified model with only the fluid-dynamics module was built with COMSOL Multiphysics to model the impinging jet flow, where a stationary and blocking substrate was used instead of the porous GDE. The flow profiles in the three flow regions characterizing impinging flow: free jet, impingement, and wall jet regions were validated against reported numerical [28] and analytical [30] solutions for Reynold numbers of Re = 1 and Re = 1000 (low and high gas flowrates). Excellent agreement was achieved between the model and the solutions reported in the literature for radial and axial flow profiles, shear stresses, and pressures as detailed in S1 section of the Supplementary Material.

4. Results and discussion

4.1. Application to stationary GDE and model calibration

As a base-case scenario, a thermal response from a stationary pristine (no defects) GDE on a bench-top roller system was used [21,25]. This experiment featured an IR camera angled at 30° to the surface of the GDE to capture the thermal response of the GDE under the knife. The knife was made of a 12.7 mm diameter stainless steel tube with 115 drilled holes of 0.5 mm diameter that were spaced 2 mm apart. The model was calibrated to capture the
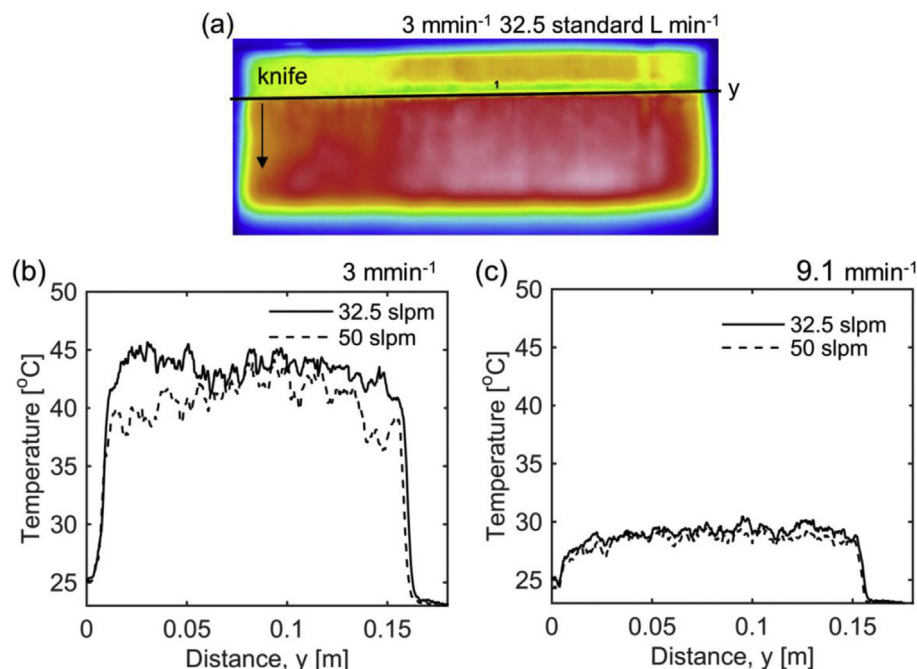
Fig. 3. a) 2D IR thermograph for a webline speed 3.0 m min^{-1}, b) cross-sectional 1D plot for webline speed 3.0 m min-1 and c) webline speed 9.1 m min^{-1} for gas flow-rates of 32.5 and 50 standard L min^{-1}.

impinging flow dynamics and thermal response. For the experimental data points shown in Fig. 2c, the temperature was averaged along the GDE at four cross-web locations spaced approximately 2 mm apart.

As Fig. 2c shows, the model captures the experimental trend well – the peak temperature and its location match, and the slope of the temperature decrease away from the impinging point is also similar. However, several model limitations have to be addressed. These include (i) model overestimation of convective cooling immediately under the injection hole because the heat redistribution along the knife in the cross-web direction is not incorporated; and (ii) the kinetic model is simplified and does not incorporate the oxygen dependence in the kinetic rate equation (only through a mass-balance) or adsorbed reaction intermediates or spectators [25].

Fig. 2d shows a sample two-dimensional plot of hydrogen concentration and flow streamlines, where the highest hydrogen concentration is at the knife exit and corresponds to 0.66 mol m^{-3}. Only half of the modeling domain is shown since, for a stationary web, the flow profile is symmetric about the impinging point. One can observe that a larger portion of hydrogen escapes from the top than permeates/diffuses through the GDE. Fig. 2e shows a two-dimensional temperature profile, where a cool spot under the knife is due to convective cooling and the hot spot is shifted to a location of 5 mm away from the impingement point. It is important to note that the IR-camera captures the temperature signature at the GDE surface, whereas the model calculates the temperature of the GDE and surrounding air.

4.2. Moving GDEs on a webline

It is to be expected that cost effective GDE materials will be manufactured on weblines. Fig. 3a shows the experimental thermal response for a pristine GDE moving at a speed of 3.0 m min^{-1}, through the webline with the gas flowrate of 32.5 standard L min^{-1}. The location of the knife edge is marked with a black line labeled

"y", which also serves as the line along which the 1D thermal profile for Fig. 3b for 32.5 standard L min^{-1} is extracted. For accurate defect detection, a uniformity of temperature along the "y" line for pristine GDE is necessary because this temperature serves as a reference temperature for defect detection. From Fig. 3b, for a gas flowrate of 32.5 standard L min^{-1}, a uniform thermal excitation is observed, whereas, for 50 standard L min^{-1}, a less uniform thermal excitation pattern is observed. From the 1D temperature profile shown, it is seen that local thermal fluctuations for the lower flowrate are smaller. To quantify thermal noise associated with the nonuniform temperature profile along the "y" line mean temperature, the standard deviation and noise-to-signal ratio for two gas flowrates and webline velocities are reported in Table 3. To calculate these values, a sample of temperature data along the "y" line was taken that encompassed 500 recorded points. For 3 m min^{-1}, the mean temperature at a gas flowrate of 32.5 standard L min^{-1} was 43.4 °C, whereas that for 50 standard L min^{-1} was 40.7 °C. Standard deviations for temperature profiles for these two gas flow-rates were 1.11 and 1.82 °C, respectively. The noise-to-signal ratio here is defined as two standard deviations divided by the mean temperature. For 32.5 standard L min^{-1} it was 5.12%, however, for 50 standard L min^{-1} it was higher at 8.97%.

For the higher substrate velocity (9.1 m min^{-1}), as Fig. 3c shows, the local temperature fluctuations for gas flowrates of 32.5 and 50

Table 3
Statistics for experimental IR thermography data for two webline speeds and two gas flow-rates.

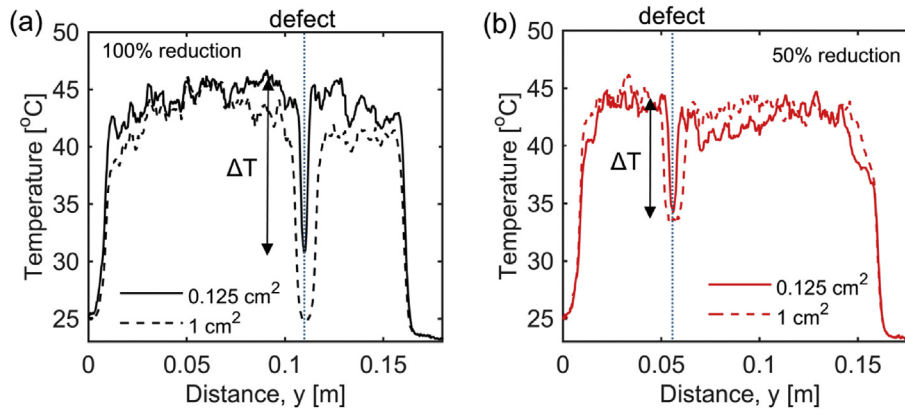| Webline speed [m min^{-1}], Gas flow-rate [standard L min^{-1}]	Mean temperature, T_m[°C]	Standard deviation, σ_{T_m} [°C]	Noise to signal percentage, $2\sigma_{T_m}T_m^{-1} \times 100$ [%]
3.0, 32	43.4	1.11	5.12
9.1, 32	29.0	0.79	5.42
3.0, 50	40.7	1.82	8.97
9.1, 50	28.4	0.83	5.85

Fig. 4. Temperature profile extracted from IR thermograph for defect areas of 0.125 and 1 cm² for a) 100% loading reduction and b) 50% loading reduction.

standard L min⁻¹ were comparable: standard deviations were 0.79 and 0.83 °C, and mean temperatures were 29.0 and 28.4 °C, respectively. The noise-to-signal ratio was very similar for both gas flowrates: 5.42 and 5.85, respectively. Comparing temperature for lower (3.0 m min⁻¹) and higher substrate velocity (9.1 m min⁻¹), the mean pristine temperature is a factor of 1.6–1.7 higher for lower and only 1.1 for higher substrate velocities compared to the ambient temperature. It is desirable to have a higher mean pristine temperature in order to maximize the temperature difference between the

pristine and defected locations. However, the tradeoff is that the noise-to-signal on average is larger for higher pristine temperatures. It is worth mentioning that for a stationary GDE, the peak temperature was 118 °C, which is a factor of 4.7 above ambient.

The corresponding model results for the above experimental conditions are shown in Fig. S7 of Supplementary Material. In good agreement with the experimental data, the GDE at a speed of 3.0 m min⁻¹ has a higher temperature at the detection point, whereas temperature for higher speed of 9.1 m min⁻¹ is lower.
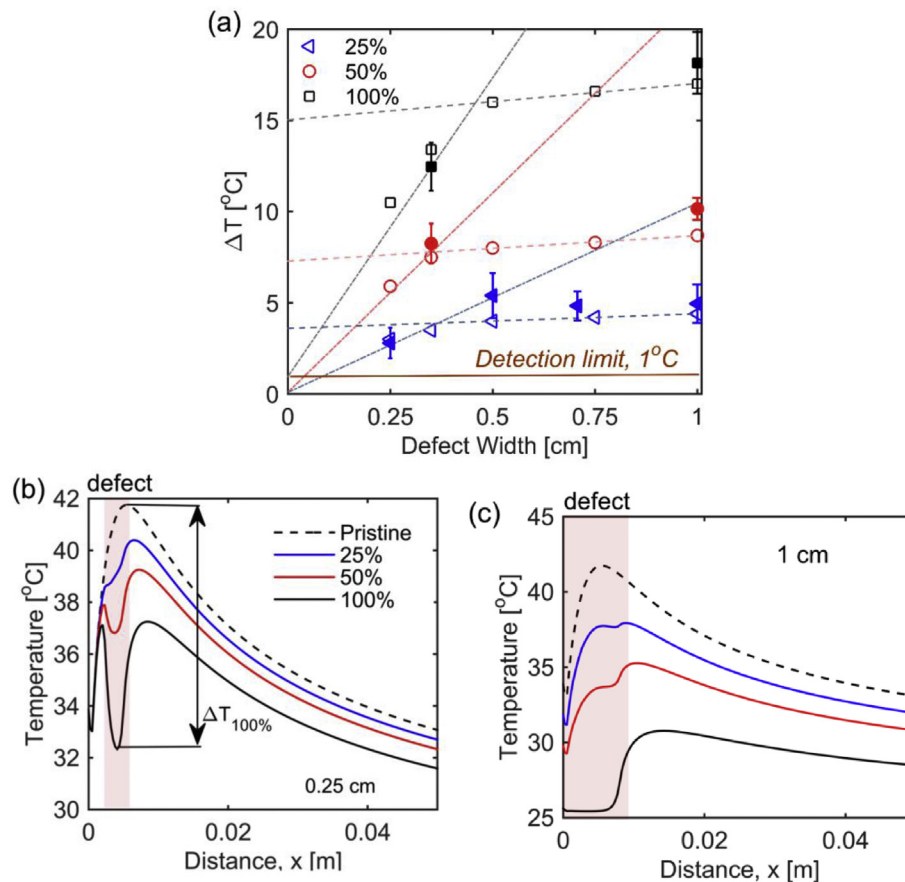

Fig. 5. a) Temperature difference across the defect as a function of defect width for defect reductions of 25%, 50% and 100% and webline speed of 3 m min⁻¹ and gas flowrate of 32 standard L min⁻¹. Spatial distribution of temperature on top of GDE are shown for b) 0.25 cm and c) 1 cm defects, where a pristine (reference) GDE is shown as a dashed line and the defect location is shaded.
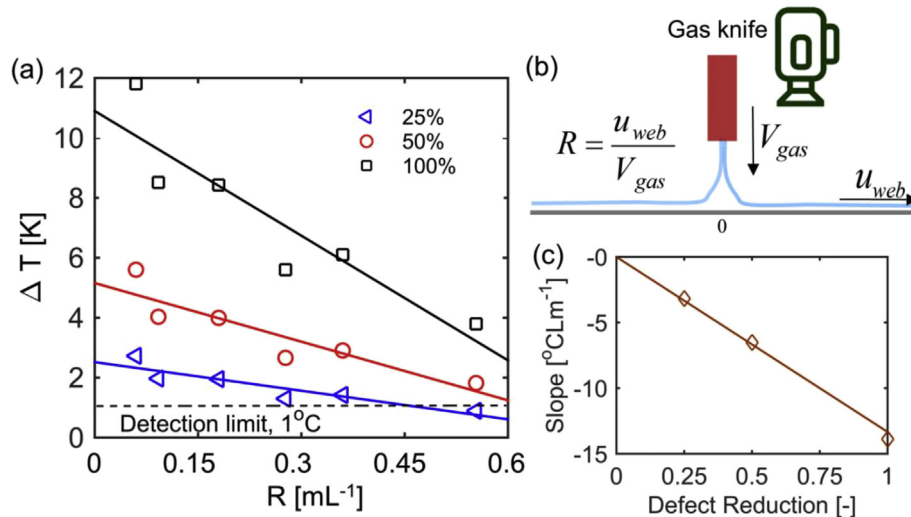
Fig. 6. a) Temperature difference between the pristine and defect (0.2 cm) locations on the GDE as a function of the ratio of webline velocity to inlet flowrate, R, for three Pt loading reductions: 25, 50 and 100%. b) A schematic illustrating the definition of R and c) slope extracted from a) as a function of defect reduction.

5. Detection of defects

Above we only considered instances when a pristine GDE with a nominal loading of 0.13 mg$_{Pt}$ cm^{-2} is either stationary or moving on the webline. In this section, experimental and modeling results are shown for the thermal response of the excited GDEs with defects on a moving webline including parametric studies to identify optimal parameter space for defect detection.

5.1. GDE defects on a moving webline

Fig. 4a shows experimental temperature profiles along the width of the GDE for defect areas of 0.125 and 1 cm^2 and 100% loading reduction (*i.e.* a bare spot) for a web speed of 3.0 m min^{-1} and a gas flowrate of 32 standard L min^{-1}. The position of the center of the defect is shown by the dotted line on the figure. The decrease in temperature, ΔT, is 18 °C for the larger defect and 13 °C for the smaller defect, where ΔT is defined as the difference between the mean GDE temperature in the defect-free locations, T_m, minus the minimum temperature at the defect location, T_{def}:

$$\Delta T = T_m - T_{def} \tag{14}$$

From Table 3 for these operation conditions, the thermal fluctuations due to the signal noise for the pristine GDE are on the order of ± 1.11 °C. Therefore both 0.125 and 1 cm^2 defects are clearly detectable. For the same experimental conditions but 50% loading reduction (0.065 mg$_{Pt}$ cm^{-2} loading), as shown by Fig. 4b, the ΔT is 10 °C for the larger defect and 8 °C for the smaller one. These are 1.8 and 1.6 times smaller compared to ΔT's for 100% defect reduction, however still much larger than the thermal fluctuations reported in Table 3 and hence detectable.

It is of interest to explore the limits of defect detectability, which is more effective to do through modeling. Fig. 5a shows ΔT as a function of defect width for Pt-loading reductions of 25, 50, and 100% and webline speed of 3 m min^{-1} and gas flowrate of 32 standard L min^{-1}. The defect widths are along the down-web dimension and here their cross-web dimension is not considered because the model is not three-dimensional; for simplicity, one may consider them to be squares. A representative detection limit of 1 °C was chosen for this analysis based on our prior work in developing thermographic inspection methods for fuel-cell

materials [22,23]; the actual limit would be set based on signal noise of a fully developed and implemented system. The model results are shown as open symbols and were fit with two linear fits. The filled symbols show experimental data for ΔT (as defined by Eq. (14)) of defects, with error bars representing plus/minus one standard deviation of mean temperature for pristine regions of the GDE in the cross-web direction. As expected, ΔT is higher for defects with higher thickness reduction. Two linear regimes are observed for the range of defect widths. For defect widths smaller than 0.5 cm, a steep increase in ΔT is observed, whereas for defect widths larger than 0.5 cm, ΔT remains approximately constant.

For smaller defects, the temperature at the defect midline is higher because of heat conduction from the neighboring pristine regions. As defects become wider, heat conduction to the center of the defect becomes smaller and hence ΔT remains approximately constant. For 100% defect reduction, these two regions are more pronounced, whereas for 25% reduction, ΔT < 5 °C for the whole range of defect widths. Using the representative detection limit of 1 °C, the model predicts that all of the defects at all of the loading reductions studied should be detectable, which is in agreement with the experimental testing. Moreover, the model suggests that the detection limit can be relaxed to 2.5 °C and the defects will still be detected with this technique. Similarly, the model predicts defect detectability limit of 0.1 cm defect width or 0.01 cm^2 defect area for the conditions in Fig 5a. This defect size is six times smaller than the smallest defect considered in the experimental study, which is indicative that the maximum detection limit of the IR thermography technique has not been reached yet and even smaller defects can be considered in future studies.

Fig. 5b and c shows the down-web temperature profile at the GDE surface for 0.25 and 1 cm defects (0.0625 and 1 cm^2, respectively), which are the smallest and the largest defects tested experimentally. The plotted loading reductions are 25, 50, and 100%, and ΔT is the temperature difference defined by Eq. (14). For the modeling study, T_m is the temperature for a pristine GDE. The same ΔT's calculated from Fig. 5b and c are plotted in Fig. 5a. The locations of the defect are shown as shaded regions. As already shown by Fig. 5a, a much larger variation in ΔT is observed for 1 cm defect compared to 0.25 cm defect. An interesting observation from the modeling study is that the temperature profile downstream from the defect location is consistently lower than the temperature of a pristine GDE. In the actual experiment, lateral heat conduction
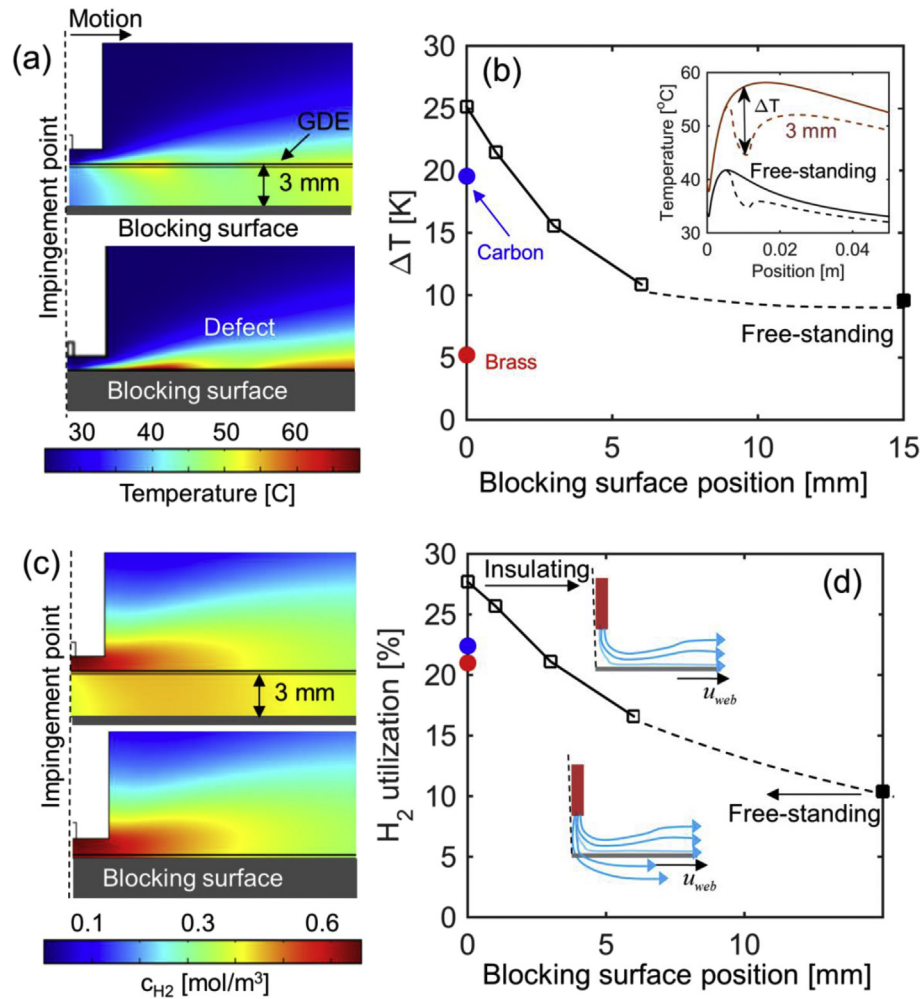
Fig. 7. a) 2D plots of temperature distribution for a webline with a solid surface placed 3 mm under the GDE and for a GDE with contacting insulating surface. Defect size is 5 mm, GDE speed 3 m min^{-1} and gas flowrate of 32 standard L min^{-1}. b) Temperature difference between pristine and 5 mm defect locations as a function of the base position, the brass, carbon bases and free-standing GDEs are shown too. c) 2D plots of hydrogen concentration distributions and d) hydrogen utilization for different substrates and positions.

and redistribution from the pristine locations should reduce this behavior.

Thus far, only a single operating condition (3 m min^{-1} and 32 standard L min^{-1}) has been discussed. However, it is of interest to understand how web speed and impinging gas flowrate affect defect detectability. For this study, six different combinations of web speed and gas flowrates were considered. The web velocities were 3.0, 9.1, and 18.3 m min^{-1}, with gas inlet flowrates of 32.5 and 50 standard L m^{-1}. A very small defect of 0.2 cm was selected. Fig. 6a shows ΔT as a function of R, where R is defined as the ratio between the web velocity, u_{web} and inlet gas flowrate, V_{gas}. As an example, for the baseline operation condition of 3 m min^{-1} and 32.5 standard L m^{-1}, R = 0.09 mL^{-1}. For each level of CL reduction, a linear fit was created through the respective modeling data points. Because both flowrate and web velocity were varied, model data points did not fall perfectly onto the linear fit. For three cases of defect loading reduction the slope varied, with steeper slopes for higher defect-loading reductions. This trend is indicative that ΔT varies with R at higher rates for higher defect-loading reduction. For example, for 100% defect reduction ΔT decreased from 8.7 to 4 °C when R increased from 0.2 to 0.55 m L^{-1}. For the range of R considered and loading reductions of 50 and 100%, ΔT is always larger than 1 °C. Therefore, if we are only interested in detecting larger defect reductions, such as 50 and 100%, then the web velocity

can be as high as 18.3 m min^{-1}, a factor of six larger than the baseline scenario. However, for 25% defect reduction, ΔT decreased from 2 °C at small values of R to less than 1 °C at R > 0.45 m L^{-1}. Thus, the model suggests that it will be critical to optimize R for detection of low-thickness reduction defects.

Fig. 6c plots the slope for ΔT vs. R for each catalyst loading reduction as a function of catalyst loading reduction. For the three defect levels, the slope is linear and becomes more negative for higher loading reductions. Knowing the slope and one model simulation point, the rest of the ΔT vs. R figure can be reproduced, allowing prediction of detectability for any defect at any value of R.

5.2. Effect of adding a blocking surface and hydrogen utilization

We look at several improvement strategies to increase ΔT and hydrogen utilization by studying the addition of a blocking surface at varying distances on the bottom of the GDE, at a fixed distance of 6 mm on top and by adding a blocking surface on both top and bottom of the GDE. The results discussed in this section are for the substrate speed of 3.0 m min^{-1} and gas flow-rate of 32 standard L min^{-1} and defect size of 5 mm, unless indicated otherwise.

Fig. 7a shows a two-dimensional temperature distribution for the GDE and surrounding air, where the top plot is for a blocking surface placed 3 mm under the GDE and the bottom plot is for a
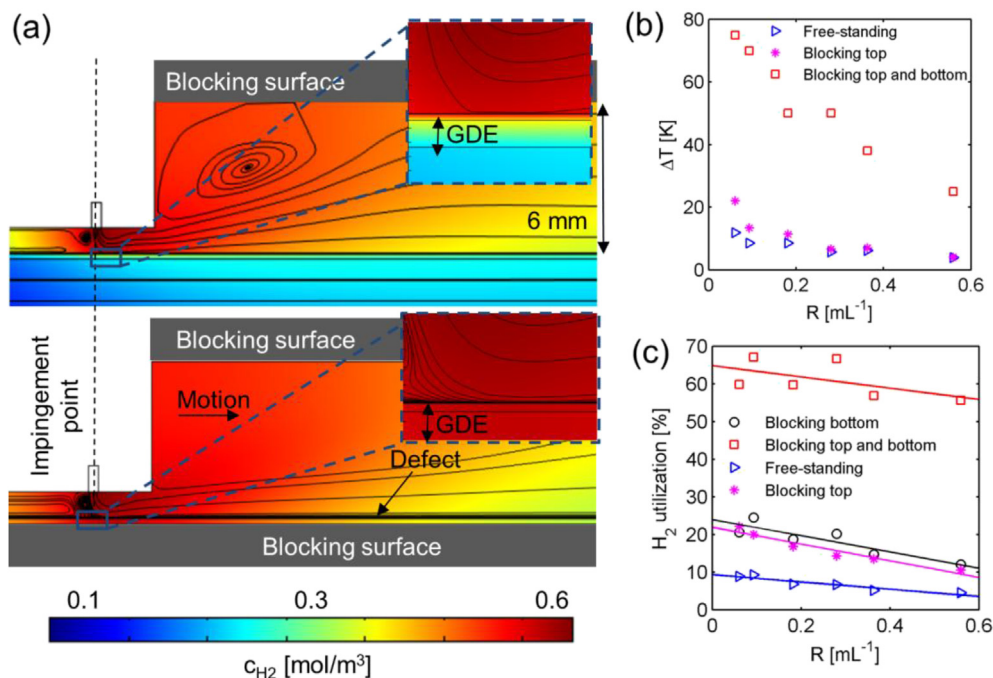
Fig. 8. a) 2D plots of hydrogen concentration distribution for a webline GDE speed of 3 m min^{-1} and gas flowrate of 32 standard L min^{-1} with a blocking surface on the top (top image) and both top and bottom (bottom image). b) ΔT as a function of R for free-standing, blocking top, and blocking top and bottom cases. c) Hydrogen utilization as a function of R for free-standing GDE, with the solid base on the top and with the solid base on the bottom and 6 mm above the GDE.

blocking surface placed in direct contact with the bottom of the GDE. In the latter scenario, the blocking surface is also acting as a perfect heat insulator as shown. To quantify these results and to extend the analysis further, carbon and brass blocking surfaces are also considered in Fig. 7b, where 0 indicates complete contact with the GDE substrate. From this figure, the highest $\Delta T = 25\ ^{\circ}$C is for an insulating base and it decreases to 10 $^{\circ}$C for a blocking surface positioned 7 mm under the GDE; removing the surface even further from the GDE, i.e. creating a "freestanding" GDE layer, does not produce significant changes to ΔT as it is far enough away to have no appreciable effect. If, instead of an insulating blocking surface, a blocking material made of carbon or brass is used (i.e., much higher thermal conductivities of 1.7 and 109 W m^{-1} K^{-1}, respectively), then ΔT values of 20 and 5 $^{\circ}$C are observed, respectively, which are 1.25 and 5 times smaller compared to the insulating case.

When the blocking surface is present, H$_2$ is forced to either react within the GDE or escape to the environment at the top as shown by Fig. 7c. Fig. 7d shows the H$_2$ utilization, which is defined as the H$_2$ reaction flux within the GDE divided by the inlet H$_2$ flux. A maximum H$_2$ utilization of 28% is achieved with the insulating surface and the lowest H$_2$ utilization of 10% is for the free-standing GDE.

The second improvement strategy considered here is placing a blocking surface 6 mm above the GDE and the third strategy was placing blocking surfaces on the top and bottom of the GDE, creating a tunnel. Fig. 8a shows the hydrogen distribution and streamlines for a blocking surface 6 mm above the GDE. The GDE is free-standing and the hydrogen concentration decreases from 0.6 mol m^{-3} near the impingement point to close to 0 underneath the GDE. Fig. 8a (bottom 2D image) shows the hydrogen concentration when an additional blocking substrate is introduced at the bottom of the GDE. The hydrogen concentrations in air above the GDEs for both studied cases are similar; however, a major difference is observed in the hydrogen concentration at the reacting layer as shown in the zoomed-in images. For the free-standing GDE, the hydrogen concentration rapidly drops within the GDE, whereas, for the GDE/

blocking surface case, the hydrogen concentration remains constant through the GDE thickness in the location under the impingement point. From Fig. 8b, having the blocking surface on top of GDE produced a higher ΔT at R < 0.2 m L^{-1}, however, no significant difference in ΔT was observed at R > 0.2 m L^{-1}. More than a four-fold increase in ΔT is observed for the case of the GDE having both top and bottom blocking surfaces (a tunnel) for a full range of R.

Practically, to utilize a blocking surface on the top of the GDE on the webline might be challenging because it can interfere with the thermal signal for IR detection. A slit opening in the solid surface or an IR-transparent material for the blocking surface are two possible solutions to ensure that the surfaces are blocking and that the IR-camera can detect the GDE's thermal response. As for the surface on the bottom of the GDE, a similar solution to the one discussed in the section above can be utilized.

6. Conclusion

Reactive impinging flow (RIF) of a H$_2$/O$_2$/N$_2$ gas mixture was used to excite Pt electrocatalysts thermally within a gas-diffusion electrode (GDE) for in-line quality-control detection using infrared (IR) thermography. The RIF setup was implemented on a research webline, where 15 GDE defects of sizes 0.0625, 0.13, 0.25, 0.5, and 1.0 cm^2 and catalyst loading reductions of 25, 50 and 100% were successfully detected at different webline speeds and gas flowrates. Mathematical modeling was conducted to identify detection limits for different web velocity and gas flowrate as a function of defect size. For a detection threshold of 1 $^{\circ}$C, the model correctly predicted that all of the experimentally studied defects should be detectable with the RIF technique. Moreover, the model predicted that much smaller defects can be detected under certain operating conditions.

A modeling study was used to design several improvement routes to achieve an even larger defect detection window and higher utilization of H$_2$ from the impinging stream. It was shown that placing a blocking substrate on top (6 mm) or at various

distances below the GDE increased ΔT and hydrogen utilization. Substrates with various thermal conductivities were studied and it was found that an ideal insulator produces the largest ΔT, whereas a blocking surface that acts as a strong heat sink lowers the ΔTs with respect to a free-standing GDE. However, the most dramatic increase in ΔT (factor of four) was achieved by placing blocking surfaces on both the top and bottom of the GDE, creating a hydrogen tunnel due to the higher hydrogen concentrations sustained within the GDE in this scenario. Future studies will explore experimentally the use of a blocking substrate that is impermeable to hydrogen to validate model predictions. Overall, the RIF technique is shown to be a promising route for in-line, high-speed, large-area detection of GDE defects on moving weblines.

Acknowledgments

Appendix A. Supplementary data

Supplementary data related to this article can be found at http://dx.doi.org/10.1016/j.jpowsour.2016.09.109.

References

[1] M.K. Debe, Nature 486 (2012) 43–51.
[2] D.E. Curtin, R.D. Lousenberg, T.J. Henry, P.C. Tangeman, M.E. Tisack, J. Power Sources 131 (2004) 41–48.
[3] R.R. Søndergaard, M. Hösel, F.C. Krebs, J. Polym. Sci. Part B Polym. Phys. 51 (2012) 16–34.
[4] T. Steenberg, H.A. Hjuler, C. Terkelsen, M.T.R. Sanchez, L.N. Cleemann, F.C. Krebs, Energy & Environ. Sci. 5 (2012) 6076–6080.
[5] V. Mehta, J.S. Cooper, J. Power Sources 114 (2003) 32–53.
[6] F. Barbir, S. Yazici, Int. J. Energ Res. 32 (2008) 369–378.
[7] in, ACI, Inc., 2012.
[8] R.J. Balliet, J. Newman, J. Electrochem Soc. 158 (2011) B927.
[9] A.Z. Weber, J. Newman, J. Electrochem. Soc. 154 (2007) B405–B412.
[10] P.K. Das, X. Li, Z.S. Liu, J. Electroanal. Chem. 604 (2007) 72–90.
[11] A.A. Kulikovsky, Int. J. Hydrogen Energy 36 (2011) 4449–4453.
[12] R. Borup, J. Meyers, B. Pivovar, Y.S. Kim, R. Mukundan, N. Garland, D. Myers, M. Wilson, F. Garzon, D. Wood, P. Zelenay, K. More, K. Stroh, T. Zawodzinski, J. Boncella, J.E. McGrath, M. Inaba, K. Miyatake, M. Hori, K. Ota, Z. Ogumi, S. Miyata, A. Nishikata, Z. Siroma, Y. Uchimoto, K. Yasuda, K.-i. Kimijima, N. Iwashita, Chem. Rev. 107 (2007) 3904–3951.
[13] A.Z. Weber, J. Newman, J. Electrochem. Soc. 153 (2006) A2205–A2214.
[14] M. Pestrak, Y. Li, S.W. Case, D.A. Dillard, M.W. Ellis, Y.-H. Lai, C.S. Gittleman, J. Fuel Cell Sci. Technol. 7 (2010), 041009–041009.
[15] S. Couse, T. Akin, in: Google Patents, 2014.
[16] R. Su, M. Kirillin, E.W. Chang, E. Sergeeva, S.H. Yun, L. Mattsson, Opt. Express 22 (2014) 15804–15819.
[17] C. Wyon, D. Delille, J.P. Gonchond, F. Heider, L. Kwakman, S. Marthon, I. Mazor, A. Michallet, D. Muyard, L. Perino-Gallice, J.C. Royer, A. Tokar, Thin Solid Films 450 (2004) 84–89.
[18] C. Wyon, J.P. Gonchond, D. Delille, A. Michallet, J.C. Royer, L. Kwakman, S. Marthon, Appl. Surf. Sci. 253 (2006) 21–27.
[19] M.A. Sapia, J.G. Clark, in: Google Patents, 1991.
[20] G.J. Lamont, D.P. Wilkinson, in: Google Patents, 2003.
[21] M. Boehmisch, C. Haas, in: Google Patents, 2006.
[22] N.V. Aieta, P.K. Das, A. Perdue, G. Bender, A.M. Herring, A.Z. Weber, M.J. Ulsh, J. Power Sources 211 (2012) 4–11.
[23] P.K. Das, A.Z. Weber, G. Bender, A. Manak, D. Bittinat, A.M. Herring, M. Ulsh, J. Power Sources 261 (2014) 401–411.
[24] D.C. Bittinat, G. Bender, J.M. Porter, M. Ulsh, ECS Trans. 58 (2013) 495–503.
[25] M. Ulsh, J.M. Porter, D.C. Bittinat, G. Bender, Fuel Cells 16 (2015) 170–178.
[26] T. Berning, D.M. Lu, N. Djilali, J. Power Sources 106 (2002) 284–294.
[27] T. Mitani, F.A. Williams, Combust. Flame 39 (1980) 169–190.
[28] M.D. Deshpande, R.N. Vaishnav, J. Fluid Mech. 114 (1982) 213–236.
[29] G.S. Hwang, A.Z. Weber, J. Electrochem. Soc. 159 (2012) F683–F692.
[30] M. Glauert, J. Fluid Mech. 1 (1956) 625–643.